

Contents

Chinese Abstract	I
English Abstract	III
Acknowledgement	V
Contents	VI
Table Captions	IX
Figure Captions	X
Chapter 1 Introduction	
1.1 Overview of Nonvolatile Memory	1
1.1.1 SONOS Nonvolatile Memory Devices.....	2
1.1.2 Nanocrystal Nonvolatile Memory Devices.....	4
1.2 Organization of This Thesis	8
Chapter 2 Basic Principle of Nonvolatile Memory	
2.1 Introduction.....	13
2.2 Basic Program/Erase Mechanisms.....	14
2.2.1 Energy band diagram during program and erase operation	14
2.2.2 Carrier injection mechanisms.....	14
2.3 Basic Reliability of Nonvolatile Memory.....	18
2.3.1 Retention.....	19
2.3.2 Endurance.....	19
2.4 Basic Physical Characteristic of Nanocrystal NVM.....	20
2.4.1 Quantum Confinement Effect.....	20
2.4.2 Coulomb Blockade Effect.....	20

Chapter 3 Formation and nonvolatile memory effect of Ni-Si-O and Ni-Si-N nanocrystal

3.1 Motivation.....32

3.2 Nonvolatile Ni-Si-O Nanocrystal Memory.....34

 3.2.1 Experimental Procedures34

 3.2.2 Results and Discussions34

3.3 Nonvolatile Ni-Si-N Nanocrystal Memory.....36

 3.3.1 Experimental Procedures36

 3.3.2 Results and Discussions.....37

3.4 Mechanism of Ni-Si-O and Ni-Si-N Nanocrystal Formation by DC Sputter at Room Temperature.....39

 3.4.1 Gibbs free energy.....39

 3.4.2 Results and Discussions.....40

3.5 Comparison of Electrical Characteristics between Ni -Si-O and Ni-Si-N Nanocrystal Nonvolatile Memory41

3.6 Summary I.....42

Chapter 4 Improved Performance of Ni-Si-O and Ni-Si-N Nanocrystal Memory by Thermal Treatment

4.1. Motivation.....55

4.2. Thermal treatment for Ni-Si-O Nanocrystal Memory.....55

 4.2.1 Experimental Procedures55

 4.2.2 Results and Discussion.....56

4.3. Thermal treatment for Ni-Si-N Nanocrystal Memory.....58

 4.3.1 Experimental Procedures58

 4.3.2 Results and Discussion.....59

4.4. Summary II.....62

Chapter 5 Multi-Layer Ni Silicide Nanocrystal Memory

5.1 Motivation.....82

5.2 Experimental Procedures82

5.3 Results and Discussion.....83

5.4 Summary III84

Chapter 6 Conclusion

6.1 Conclusions.....89

References.....91



Table Captions

Chapter 3

Table 3-1 Comparisons of memory window and nanocrystal density between two type nonvolatile memory devices.

Table 3-2 Comparisons of retention between two type nonvolatile memory devices.

Chapter 4

Table 4-1 Comparisons of memory characteristics for Ni-Si-O nanocrystal memory before and after RTA annealing in N₂.

Table 4-2 Comparisons of memory characteristics for Ni-Si-N nanocrystal memory before and after RTA annealing in N₂.

Table 4-3 Endurance properties of NiSi nanocrystal embedded in SiO_x and SiN_x after RTA process at 600 °C.

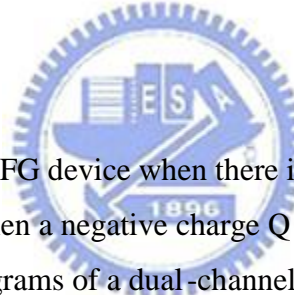
Table 4-4 Summary of memory characteristics for nanocrystal memories in our work.

Figure Captions

Chapter 1

- Figure 1-1 The structure of the conventional floating gate nonvolatile memory device. Continuous poly-Si floating gate is used as the charge storage element.
- Figure 1-2 The development of the gate stack of SONOS EEPROM memory devices. The optimization of nitride and oxide films has been the main focus in recent years.
- Figure 1-3 The structure of the SONOS nonvolatile memory device. The nitride layer is used as the charge-trapping element.
- Figure 1-4 The structure of the nanocrystal nonvolatile memory device. The semiconductor nanocrystals or metal nanocrystals are used as the charge storage element instead of the continuous poly-Si floating gate.

Chapter 2

- 
- Figure 2-1 I-V curves of an FG device when there is no charge stored in the FG (curve A) and when a negative charge Q is stored in the FG (curve B).
- Figure 2-2 Energy band diagrams of a dual-channel SONOS transistor under (a) program (b) erase operation. electrons, holes.
- Figure 2-3 (a) Schematic cross-section of nanocrystal memory device structure; (b) illustration of write process: inversion-layer electron tunnels into the nanocrystal; (c) illustration of erase process: accumulation layer hole tunnels into the nanocrystal, electron in nanocrystal can tunnel back to the channel.
- Figure 2-4 Fourth approaches to programming methods, described by Hu and White. (a) Direct tunneling (DT) (b) Fowler-Nordheim tunneling (FN) (c) modified Fowler-Nordheim tunneling (MFN) (d) trap assistant tunneling (TAT).
- Figure 2-5 Schematic cross section of MOSFET. The energy-distribution function at point (X_1, Y_1) is also shown.

- Figure 2-6 A schematic energy band diagram describing the process involved in electron injection.
- Figure 2-7 Energy-band diagram for the proposed band to band induce hot electron injection mechanism and schematic illustration cross of the Flash memory with p-channel cell. Due to the positive bias to the control gate, holes are not injected into the tunnel oxide.
- Figure 2-8 Band to band induce hot hole injection mechanism and schematic illustration cross of the Flash memory with p-channel cell.
- Figure 2-9 A typical result of an endurance test on a single cell. Threshold voltage window closure as a function of program / erase cycles on a single cell.
- Figure 2-10 Anomalous SILC modeling. The leakage is caused by a cluster of positive charge generated in the oxide during erase. The multitrapped assisted tunneling is used to model SILC: trap parameters are energy and position.

Chapter 3

- Figure 3-1 Schematics of the experimental procedures. (a) Oxygen deficient $\text{Ni}_{0.3}\text{Si}_{0.7}$ layer and (b) Oxygen incorporated $\text{Ni}_{0.3}\text{Si}_{0.7}$ layer as charge trapping layer.
- Figure 3-2 Cross-sectional TEM images of the MOIOS structure with (a) oxygen deficient $\text{Ni}_{0.3}\text{Si}_{0.7}$ layer and (b) oxygen incorporated $\text{Ni}_{0.3}\text{Si}_{0.7}$ layer, respectively.
- Figure 3-3 Capacitance-voltage (C-V) hysteresis of the fabricated MOIOS structure with (a) oxygen deficient $\text{Ni}_{0.3}\text{Si}_{0.7}$ layer and (b) oxygen incorporated $\text{Ni}_{0.3}\text{Si}_{0.7}$ layer.
- Figure 3-4 (a) Ni 2*p* XPS analysis of the oxygen incorporated $\text{Ni}_{0.3}\text{Si}_{0.7}$ layer. The peak position and profile of Ni 2*p*_{3/2} are similar to Ni-Si-O signal. (b) O 1*s* XPS analysis of the oxygen incorporated $\text{Ni}_{0.3}\text{Si}_{0.7}$ layer. Empty circles and straight line indicate experimental and fitting results, respectively. The main peak can be composed into two components which center at 531.5 eV and 532.4 eV corresponding to Ni-Si-O bond and Si-O-Si bond, respectively.
- Figure 3-5 Data retention characteristics of the nonvolatile Ni-Si-O nanocrystal

memory at room temperature.

- Figure 3-6 Endurance characteristics of the nonvolatile Ni-Si-O nanocrystal memory.
- Figure 3-7 Schematics of the experimental procedures. Nitrogen incorporated $\text{Ni}_{0.3}\text{Si}_{0.7}$ layer was fabricated as charge trapping layer. Figure 3-8 cross-sectional TEM image of the MOIOS structure with nitrogen incorporated $\text{Ni}_{0.3}\text{Si}_{0.7}$ layer.
- Figure 3-9 (a) Ni $2p$ XPS analysis of the nitrogen incorporated $\text{Ni}_{0.3}\text{Si}_{0.7}$ layer. The Ni $2p_{3/2}$ peak can be assigned to Ni-Si-N ternary bond. (b) N $1s$ XPS analysis of the charge trapping layer. Empty circles and straight line indicate experimental and fitting results, respectively.
- Figure 3-10 Capacitance-voltage (C-V) hysteresis of the fabricated MOIOS structure with Ni-Si-N nanocrystal embedded in SiN_x .
- Figure 3-11 Data retention characteristics of the Ni-Si-N nanocrystal memory at room temperature.
- Figure 3-12 Endurance characteristics of the Ni-Si-N nanocrystal memory.
- Figure 3-13 Cross-sectional TEM image of (a) oxygen and nitrogen deficient $\text{Ni}_{0.3}\text{Si}_{0.7}$ layer (b) oxygen incorporated $\text{Ni}_{0.3}\text{Si}_{0.7}$ layer (c) nitrogen incorporated $\text{Ni}_{0.3}\text{Si}_{0.7}$ layer (without capping oxide by PECVD).
- Figure 3-14 The current density-voltage (J-V) characteristics of the MOIOS structure with different charge trapping layer.

Chapter 4

- Figure 4-1 Schematics of the experimental procedures. Additional rapid thermal annealing is applied before PECVD deposition
- Figure 4-2 Capacitance-voltage (C-V) hysteresis of Ni-Si-O nanocrystal embedded in SiO_x after RTA at (a) 500 °C for 100 sec and (b) 600 °C for 100 sec.
- Figure 4-3 Cross-sectional TEM images of the Ni-Si-O nanocrystals embedded in SiO_x after RTA at (a) 500 °C for 100 sec and (b) 600 °C for 100 sec.
- Figure 4-4 The current density-voltage (J-V) characteristics of MOIOS structure with Ni-Si-O nanocrystals embedded in SiO_x before and after RTA treatment.
- Figure 4-5 XPS analysis of Si $2p$ spectra for the Ni-Si-O nanocrystals embedded in

SiO_x before and after RTA. The peak signal of Si–O bonding increased and shifted toward higher binding energy after the RTA treatment.

Figure 4-6 Charge retention characteristics of the Ni-Si-O nanocrystal memory after RTA at (a) 500 °C for 100 sec and (b) 600 °C for 100 sec.

Figure 4-7 Endurance characteristics of the Ni-Si-O nanocrystal memory after RTA at (a) 500 °C for 100 sec and (b) 600 °C for 100 sec.

Figure 4-8 Schematics of the experimental procedures. Additional rapid thermal annealing is applied before PECVD deposition

Figure 4-9 Capacitance-voltage (C-V) hysteresis of Ni-Si-N nanocrystal embedded in SiN_x after RTA at (a) 500 °C for 100 sec and (b) 600 °C for 100 sec.

Figure 4-10 Cross-sectional TEM images of the Ni-Si-N nanocrystals embedded in SiN_x after RTA at (a) 500 °C for 100 sec and (b) 600 °C for 100 sec.

Figure 4-11 The current density-voltage (J-V) characteristics of MOIOS structure with Ni-Si-N nanocrystals embedded in SiN_x before and after RTA treatment.

Figure 4-12 The XPS analysis of N 1s spectra for Ni-Si-N nanocrystals embedded in SiN_x before and after RTA. After the RTA process, the peak signal of Si–N bonding shifted toward higher binding energy. In addition, the peak signal of Ni-N decreases.

Figure 4-13 Retention characteristics of the Ni-Si-N nanocrystal memory after RTA at (a) 500 °C for 100 sec and (b) 600 °C for 100 sec.

Figure 4-14 Endurance characteristics of the Ni-Si-N nanocrystal memory after RTA at (a) 500 °C for 100 sec and (b) 600 °C for 100 sec.

Figure 4-15 (a) The simulation for electric field distribution of metal NC embedded in SiO_x. (b) The simulation for electric field distribution of metal NC embedded in SiN_x.

Figure 4-16 Charge transition under Program/Erase operation for the MOIOS structure containing NiSi nanocrystals embedded in (a) SiO_x and (b) SiN

Chapter 5

Figure 5-1 Schematics of key process steps for multi-layer Ni silicide nanocrystal memory.

Figure 5-2 Cross-sectional TEM image of multi-layer NiSi nanocrystal structure.

Figure 5-3 Capacitance-voltage (C-V) hysteresis of multi-layer NiSi nanocrystal memory.

Figure 5-4 Retention characteristics of the multi-layer NiSi nanocrystal memory as compared with single-layer NiSi nanocrystal memory at (a) 27 °C and (b) 85 °C.

Figure 5-5 Endurance characteristics of the multi-layer NiSi nanocrystal memory.

